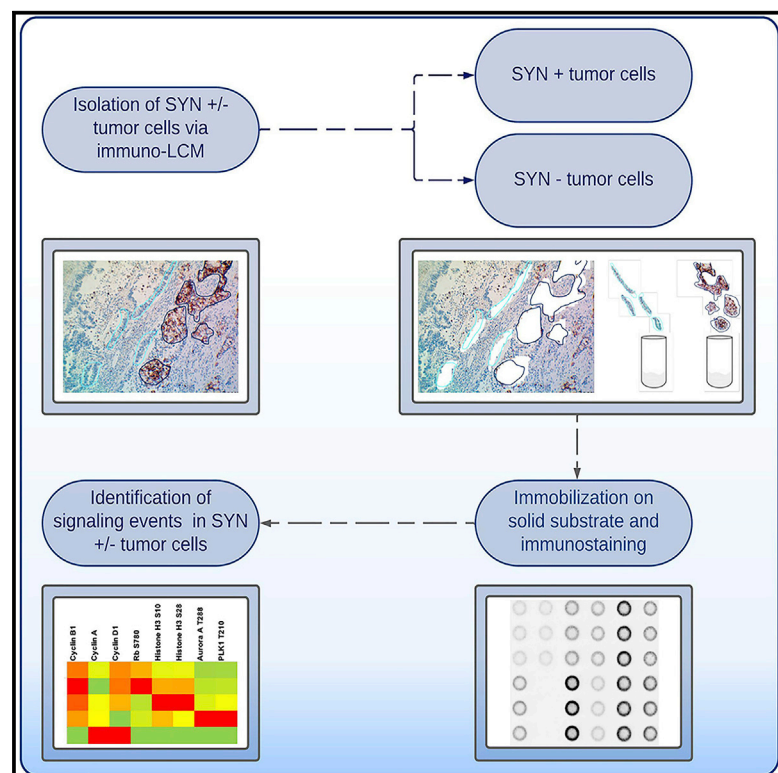**Report**

Analysis of neuroendocrine clones in NSCLCs using an immuno-guided laser-capture microdissection-based approach

Graphical abstract

Authors

Elisa Baldelli, Martina Mandarano, Guido Bellezza, Emanuel F. Petricoin III, Mariaelena Pierobon

Correspondence

mpierobo@gmu.edu

In brief

Capturing and analyzing coexisting clones in tumors is technically challenging. Here, Baldelli et al. present a workflow of immuno-guided laser-capture microdissection coupled with a reverse-phase protein microarray to measure the activation of low abundant drug targets in coexisting clones in non-small cell lung cancers.

Highlights

- Immuno-guided LCM can be used to isolate coexisting clones from complex tissue samples

- Activation of low abundant drug targets in isolated subclones can be measured by RPPA

- Signaling profiles of coexisting clones can be driven by genomic-independent events

CelPress

Cell Reports Methods

Report

Analysis of neuroendocrine clones in NSCLCs using an immuno-guided laser-capture microdissection-based approach

Elisa Baldelli,[1,4] Martina Mandarano,[1,2,4] Guido Bellezza,[2] Emanuel F. Petricoin III,[1,3] and Mariaelena Pierobon[1,3,5,*]

[1]Center for Applied Proteomics and Molecular Medicine, George Mason University, Manassas, VA, USA
[2]Department of Medicine and Surgery, Section of Anatomic Pathology and Histology, University of Perugia, Perugia, Italy
[3]School of Systems Biology, George Mason University, Manassas, VA, USA
[4]These authors contributed equally
[5]Lead contact
*Correspondence: mpierobo@gmu.edu
https://doi.org/10.1016/j.crmeth.2022.100271

MOTIVATION Coexisting clones within a tumor microecology lead to tumor heterogeneity and modulate response to treatment. Capturing protein-based signal-transduction events and druggable alternations within these clones remains challenging from a technical perspective. To address this issue, we have developed an immune-guided laser-capture microdissection workflow coupled with a reverse-phase protein microarray to isolate coexisting and underrepresented clones within the tumor microenvironment and generate functional kinase-based signaling profiles.

SUMMARY

Clonal evolution and lineage plasticity are key contributors to tumor heterogeneity and response to treatment in cancer. However, capturing signal transduction events in coexisting clones remains challenging from a technical perspective. In this study, we developed and tested a signal-transduction-based workflow to isolate and profile coexisting clones within a complex cellular system like non-small cell lung cancers (NSCLCs). Cooccurring clones were isolated under immunohistochemical guidance using laser-capture microdissection, and cell signaling activation portraits were measured using the reverse-phase protein microarray. To increase the translational potential of this work and capture druggable vulnerabilities within different clones, we measured expression/activation of a panel of key drug targets and downstream substrates of FDA-approved or investigational agents. We isolated intermixed clones, including poorly represented ones (<5% of cells), within the tumor microecology and identified molecular characteristics uniquely attributable to cancer cells that undergo lineage plasticity and neuroendocrine transdifferentiation in NSCLCs.

INTRODUCTION

The introduction of targeted anti-cancer drugs has revolutionized treatment in oncology. Even so, the therapeutic effects of targeted approaches are often temporary, as tumor cells commonly acquire resistance through clonal evolution and adaptation to altered microenvironments and therapeutic effects (Worsley et al., 2016). Among these adaptive responses, neuroendocrine (NE) transdifferentiation (TD) and histological switch (HS) are emerging as shared mechanisms of acquired resistance and poor prognosis across epithelial tumors of different origins (Farrell et al., 2017; Kleist and Poetsch, 2015; Marcoux et al., 2018; Patel et al., 2019; Sekkate et al., 2021; Shia et al., 2002; Vlachostergios and Papandreou, 2015). Deciphering the molec-ular events that define NE-TD/HS and identifying druggable vulnerabilities of these aggressive subclones is emerging as a priority in cancer research and treatment (Rubin et al., 2020).

NE lineage plasticity and HS as a mechanism of resistance to treatment in cancer has been described mostly in castration-resistant prostate cancers and epidermal growth factor receptor (EGFR) mutant non-small cell lung cancers (NSCLCs) (Quintanal-Villalonga et al., 2020; Shaurova et al., 2020; Tiwari et al., 2020). Complementary data from these two distinct tumor types have demonstrated that emerging NE-like cells retain the molecular characteristics and features of the primary tumors, such as somatic driver mutations and markers of adenocarcinomas (Lee et al., 2017; Oser et al., 2015). Recent data suggest that NE-TD and HS almost exclusively manifest in pre-existing and

initially underrepresented subpopulations of cancer cells in response to selective pressure in a favoring microenvironment (Quintanal-Villalonga et al., 2020). In NSCLCs, NE-TD and HS have mostly been reported in EGFR mutant tumors. However, it has recently been described in patients treated with EML4/ALK and immuno-checkpoint inhibitors, suggesting that NE-TD may be a broader mechanism of resistance than previously realized (Arakawa et al., 2020; Bar et al., 2019; Fujita et al., 2016; Miura et al., 2020; Sehgal et al., 2020). The number of patients diagnosed with NE-TD and HS is expected to escalate significantly in the years to come due to increased awareness of these mechanisms of resistance and a broader use of targeted inhibitors designed to overcome on-target resistance (Rubin et al., 2020).

According to the World Health Organization recommendations, the presence of NE+ cells in NSCLCs should not be routinely examined unless an NE morphology is also detected (Travis et al., 2021). However, Roper et al. have recently reported that NE-TD in EGFR mutant NSCLCs resistant to Osimertinib can be found in the absence of HS and that the clinical outcome of transdifferentiated tumors without HS matches those of patients with an SCLC transdifferentiated phenotype (Roper et al., 2020). This suggests that NE-TD without HS most likely represents an earlier event in NE clonal selection with potentially important diagnostic and clinical implications.

From a biological perspective, NE transdifferentiated NSCLCs and primary SCLCs present with similar morphological and molecular characteristics (Lee et al., 2017; Marcoux et al., 2018; Niederst et al., 2015; Nyquist et al., 2020; Offin et al., 2019; Quintanal-Villalonga et al., 2020, 2021; Sherr and McCormick, 2002). While intense research efforts have attempted to capture molecular events associated with NE-TD/HS in cancer, most of the genetic changes identified along with many RNA-based biomarkers of lineage plasticity still remain largely "undruggable" targets (Crea et al., 2016; Ostano et al., 2020; Ramnarine et al., 2019).

Laser-capture microdissection (LCM) is a sample enrichment tool for tissue-based biomarker analyses and precision medicine studies (Espina et al., 2007; Liotta et al., 2021). A recent study by Rajaram et al. is an excellent example of how LCM-based enrichment from small amounts of biological material (∼2,500 cells) can recover sufficient and well-preserved amounts of DNA and RNA for next-generation sequencing analyses (Rajaram et al., 2019). Microdissection techniques, including LCM, are a growing component of clinical next-generation sequencing (NGS) workflows and have recently been assigned CPT codes (e.g., 88380 and 88381), confirming their significance in clinical studies and practice. In brief, LCM allows the isolation, under direct visualization, of cell subpopulations from complex and heterogeneous tissues for downstream genomic, transcriptomic, and proteomic analyses (Espina et al., 2006). Cells are commonly identified based on histomorphological characteristics. However, when morphology or histologic characteristics alone are insufficient to guide accurate isolation of cell subpopulations, cell immunophenotyping via immunohistochemistry (IHC) can be used to guide sample enrichment via LCM. This technique, known as immuno-LCM, has been used in a handful of studies to capture immune cell subpopulations within the tu-

mor microenvironment (Buckanovich et al., 2006; Chai et al., 2018; Fend et al., 1999) or subgroups of cells within the nervous system (Demarest et al., 2012; Macdonald et al., 2008; Simpson et al., 2018; Tagliafierro et al., 2016). Transcriptional profiling and mass-spectrometry-based downstream analyses have been successfully coupled with immuno-LCM analysis (Rupp et al., 2006; Liu et al., 2010). Buckanovich et al. and Chabrat et al. have shown that immuno-LCM protocols can be adapted to successfully prevent RNA degradation and hydrolysis during the sample enrichment process (Buckanovich et al., 2006; Chabrat et al., 2015). Thus, this approach is suitable for multi-omic-based investigations. Given the urgency to find tools to dissect tumor heterogeneity and clonal evolution in cancer, we have conducted a proof-of-concept analysis to assess the feasibility of using immuno-LCM as an enrichment method to isolate underrepresented clones within the tumor ecology and capture the activity of FDA-approved targets and downstream substrates. Although the RPPA is not the only platform that can be coupled with immuno-LCM for molecular analyses of different clones, we selected this immunoassay for our readout because, as a proteomic technique, it does not rely on amplification of the input material and can directly capture low-abundant kinases hard to dissect in mass-spectrometry-based analyses (Gallagher and Espina, 2014). Our work demonstrated that coexisting and heterogeneously distributed clones within a tumor specimen, in our case NE-like cancer cells within NSCLCs, can successfully be isolated using immuno-LCM and be used for molecular profiling (Figure 1A). To our knowledge, this is the first study where an immuno-LCM-based workflow has been used to dissect molecular profiles, and kinase-driven signaling networks specifically, of coexisting clones in patient-derived tissue samples.

RESULTS

SYN+ and SYN− clones are present in surgical biospecimens collected from patients with NSCLC

We first measured synaptophysin (SYN) expression by IHC on two independent sets of NSCLCs comprising 238 samples, of which 50 were surgical specimens prospectively collected from chemonaïve patients with NSCLC and 188 were retrospective cases analyzed in a tissue microarray (TMA) format. Surgical specimens included stage I–IV tumors, and samples included in the TMA were collected from patients affected by stage I–III NSCLCs. Clinical, pathological, and outcome data are available for the first set only (Table S1). SYN+ malignant cells in sets 1 and 2 were identified using IHC following a standardized protocol commonly used for the diagnosis of SCLCs. In set 1, nine samples (18%) contained SYN+ malignant cells, of which seven were adenocarcinomas (77%) and two were squamous cell carcinomas (22%) (Tables S1 and S2). Of the 188 cases included on the TMA, only 6 (3.2%) presented with SYN+ tumor cells including four adenocarcinomas (66%) and two squamous (44%) cell carcinomas. Staining intensity across the 238 samples ranged between 1 and 3 and percentage of positive cancer cells between <0.2% and 40% (Tables S2 and S3). SYN+ cells were mostly found in clusters that were located at the aggressive edge of the tumor in 33% of cases or within the air spaces in
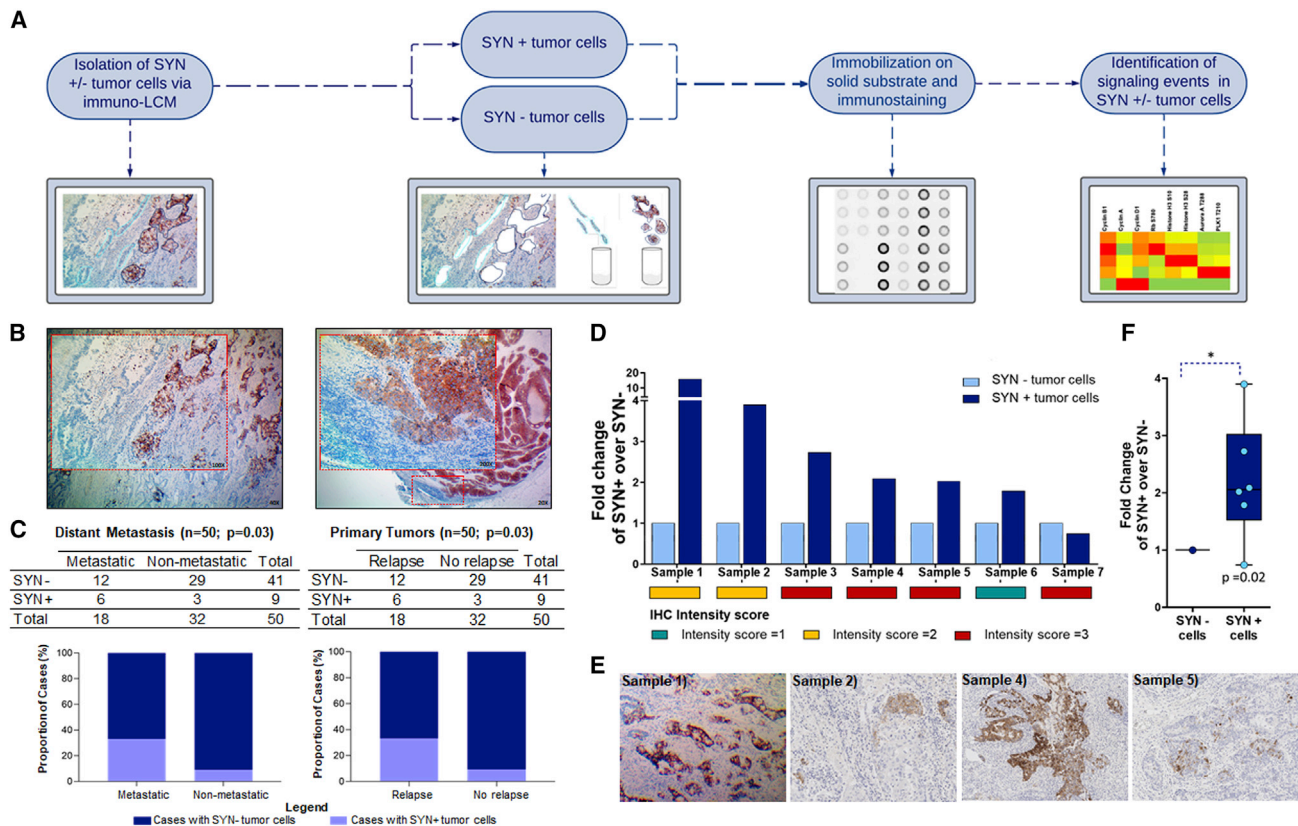
Figure 1. Study workflow and clinical-pathological and molecular characteristics of SYN+ NSCLCs

(A) Diagram capturing the steps of the immuno-LCM workflow developed for this study. SYN+ clones were first identified using standard IHC. SYN+ and SYN− clones were isolated under direct visualization using an infrared (IR)-based LCM system. Expression/activation of 57 signal transduction molecules were measured on a continuous scale using the RPPA and compared across different clones to identify signaling events that were uniquely attributable to SYN+ cells.

(B) Examples of SYN+ cells identified by IHC in a primary tumor (left site) and a lymph node metastasis (right panel) in patients with NSCLC; SYN+ cells differ in degrees of distribution: from a few to 70% of metastatic cells.

(C) Higher rates of distant metastases (p = 0.03), recurrence (p = 0.03), and poorer prognosis (p = 0.05) were detected in patients whose tumor contained SYN+ cells. Bar graph illustrating frequency of distant metastases and outcome of patients with NSCLC with and without SYN+ neuroendocrine-like cells.

(D) Bar graphs displaying changes in SYN expression in microdissected matched SYN+ and SYN− cancer cells. IHC intensity staining for each sample is reported along with the RPPA-based fold change values.

(E) Selected examples of IHC staining matching the samples displayed in the bar graph in (D).

(F) Boxplot illustrating significant changes in SYN expression between matched SYN+ and SYN− microdissected clones (p = 0.02).

11% of cases (Figures S1A and S1B). For 23 of the 50 cases, SYN expression was also evaluated in matched lymph node metastases (Table S3). Of the 23 lymph node metastases, 5 had SYN+ cells. In four cases, SYN+ cancer cells were present in both primary tumors and matched lymph node metastases, which affected patients' outcome (Figures 1B and 1C).

Matched SYN+ and SYN− clones can be successfully isolated from complex tissue samples using immuno-guided LCM

Of the 238 samples screened for this analysis, 15 had SYN+ cells. However, in seven samples, the amount of SYN+ cells per tissue section was less than 1% (Table S3), and the number of cells per section ranged between 6 and 60. A few examples are shown in the Figures S1C–S1E. Of note, such small numbers of cells are difficult to profile even for single-cell technologies and digital spatial profiling platforms (Lähnemann et al., 2020).

Eight of the 15 samples (53%) had at least 1% SYN+ cells in each tissue section and were included in this pilot analysis. SYN+ staining intensities in these samples ranged from 1 to 3, and the percentage of positive cells was between 1% and 70% (Table S3). SYN+ and SYN− subclones within the same tissue section were then isolated using immuno-guided LCM. In brief, freshly cut slides were stained using a mouse anti-SYN antibody following a standardized IHC protocol. SYN+ and SYN− clones were immediately isolated under direct microscopic visualization (Figure 1A). SYN− tumor cells were isolated at an average distance of 500 μm from SYN+ cells (Figure 2). When SYN+ cells were found in clusters, the external margin of the cluster was used as a reference point for capturing SYN− cells. Cell lysates were then immobilized onto 65 nitrocellulose-coated glass slides using an automated system and probed with 57 antibodies targeting unmodified or post-translationally modified epitopes.
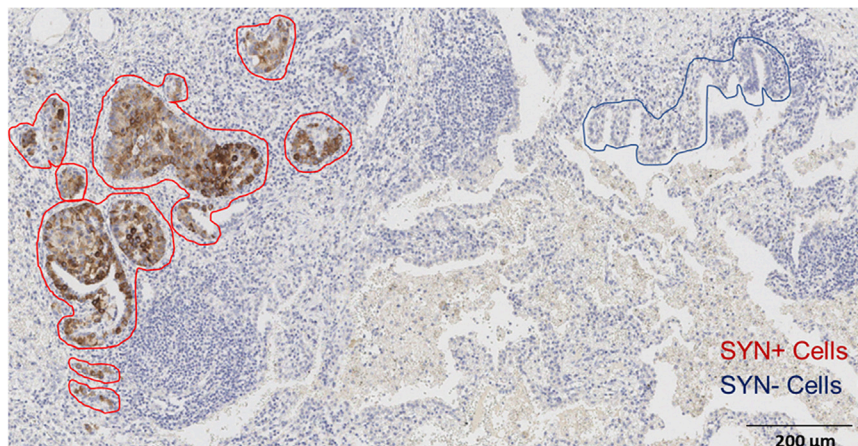
Using a rabbit anti-SYN antibody, we first assessed whether our method can successfully be used to isolate coexisting clones within the same tissue sample. As expected, the SYN amount was significantly higher in the SYN+ clone, with SYN expression increasing up to 3.9-fold compared with matched SYN− tumor cells (p = 0.02) (Figure 1F). SYN expression for individual cases is shown in Figures 1D, 1E, and S2. To assess whether the addition of the IHC step to the LCM process affects non-specific background signal on the RPPA, for one sample with a high percentage of SYN+ cells (70%) (Figure S3A), we compared the background signal generated by cells collected using a standard LCM protocol with those isolated using the developed immuno-LCM workflow. The addition of the IHC step to the LCM process did not affect the background signal of the RPPA data once the data were normalized to the total number of shots collected (Mann-Whitney U test; p > 0.05; Figure S3B). Next, we compared protein yield between the immuno-LCM sample and a cohort of formalin-fixed paraffin-embedded (FFPE) core needle biopsies collected from patients with NSCLC where tumor cells were isolated with a standard LCM protocol (Espina et al., 2007). As shown in the Figure S3C, protein yield for immuno-LCM samples, although at the lower end of a reference curve, was within the detection range of the microdissected sample and above the internal controls (Baldelli et al., 2017). Taken together, these data suggest that immuno-guided LCM can be used to isolate coexisting clones within the same tissue section providing a tool for exploring molecular events between coexisting subpopulations of tumor cells.

SYN+ cells are characterized by unique signaling profiles compared with matched SYN− tumor cells

We next quantified signaling events in SYN+ and SYN− clones using the RPPA on cell lysates generated from six of the dissected samples (samples 2–7). Our analysis focused on post-translationally modified proteins known to be involved in tumorigenesis, drug targets and downstream substrates of FDA-approved or investigational agents, and molecules known to be involved in NE-TD in cancer. While RPPA intra- and inter-assay reproducibility has been previously described (Rapkiewicz et al., 2007; Pierobon et al., 2014), coefficient of variations be-

tween technical replicates (n = 3) ranged between 1% and 15.9% across the 57 analytes measured by the RPPA.

We used unsupervised hierarchical clustering analysis to capture patterns across samples (Figure 3A). Of interest, matched SYN+ and SYN− cells collected from the same patient clustered together only for one of the six samples (Figure 3A, dark green sample). From a biological perspective, SYN+ cancer cells from different patients were mostly contained within the same cluster (Figure 3A, red branches of the dendrogram). These samples were characterized by increased phosphorylation of Rb at the S780 residue, which translates into reduced activity of the tumor suppressor, a molecular event known to be associated with NE-TD in cancer and in SCLC carcinogenesis (Quintanal-Villalonga et al., 2020, 2021). Decreased Rb activity was detected in five of the six samples in the SYN+ tumor cells compared with matched SYN− (Figures 3A, 3C, and S4A), and this reduction was statistically different (p = 0.02) even in such a small sample set (Figures 3B and 3C). Taken together, these data indicate that SYN+ and SYN− clones, even within the same tumor, have unique molecular profiles. The ability to isolate and profile them as unique entities may offer novel opportunities for understanding NE-TD in cancer and for identifying early events potentially preceding HS.

Expression and activation of known regulators of NE-TD differ between matched SYN+ and SYN− tumor cells

We then calculated the fold change between matched SYN+ and SYN− clones of each of the 57 proteins measured by RPPA and focused on analytes that showed similar directionality in four or more samples (Figures 3B, 3C, and S4A). AKT and Cdk6 were increased in the SYN+ clones compared with their SYN− counterparts in all six samples (Figures 3B, 3C, and S4A). Expression of the AKT downstream substrates 4EBP1 and beta-catenin was also increased in the SYN+ component for five of the six samples. Expression and post-translationally modified cell-cycle regulators like Cdk2, Cdk4, and Rb phosphorylated at the S780 residue, along with proteins involved in DNA-damage repair, including ATM S1981, Chk1 S345, and Chk2 S33/35, were also increased in the SYN+ clone compared with the SYN− cancer cells. In this small population of samples, selected changes like phosphorylation of Rb S780 and expression of Cdk6 reached statistical significance, with Rb S780 retaining its significance even when a pairwise comparison was conducted (Figures 3B and 3C). Lastly, the fold change between matched samples showed increased expression and activation
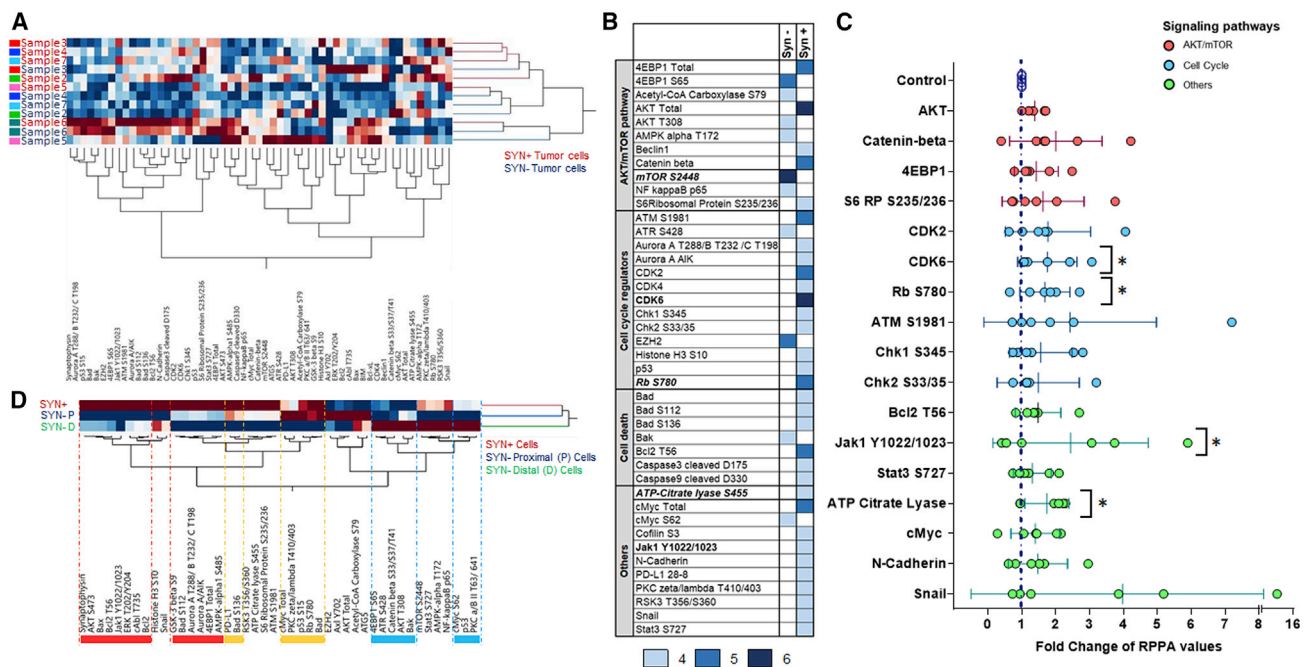
Figure 3. Expression and activation of 57 signaling molecules in matched SYN+ and SYN− clones isolated from the same tissue section

(A) Unsupervised hierarchical clustering analysis using the Ward's method of matched SYN+ and SYN− clones. Intensity values are displayed on a scale ranging from burgundy to blue, where burgundy indicates high levels and dark blue indicates low levels of expression/activation. On the x axis are listed proteins measured by RPPA; on the y axis are displayed SYN+ (red) and SYN− (blue) clones. Matched samples are identified by the same color on the left side of the panel.

(B) List of proteins that increased in four or more samples in matched SYN+ and SYN− cancer cells. Proteins that were increased in four, five, or six samples are color coded in red, blue, and green, respectively. Proteins that were statistically different between SYN+ and SYN− cancer cells are indicated in bold. Samples where significance was retained in pairwise comparisons are indicated in italic.

(C) Box plot displaying mean and 95% confidence intervals of fold change in SYN+ cancer cells compared with the SYN− clone. Asterisks highlight changes that were statistically significant; proteins were color coded based on their function.

(D) Unsupervised hierarchical clustering analysis using the Ward's method for one case where SYN+ cancer cells (red) were isolated along with proximal (blue) and distal (green) SYN− cells. Proteins are grouped based on their expression/activation across the three matched samples; in the red box are grouped proteins that increased in SYN− cells, in yellow the one increased in SYN+ and proximal SYN− cells, and in blue the one increased in distal SYN− cells.

---

of transcription factors like c-Myc and STAT3 S727, along with its regulator Jak1 post-translationally modified at the Y1022/1023 residue (Figures 3B and 3C). Because many of the molecules emerging as differentially expressed or activated in this analysis are known modulators of NE-TD in tumors of epithelial origin, this proof-of-concept study confirms that the workflow proposed may be a tool for capturing and comparing signaling events from coexisting clones within the complex tissue microecology of human biospecimens.

Interactions between signal transduction molecules differ between matched SYN+ and SYN− tumor cells

To capture the degree of interactions between signaling molecules in SYN+ and SYN− clones, we next used the continuous RPPA data to calculate pairwise correlation coefficients across all 57 analytes. To display interconnections with a high degree of association, we generated network maps that included only interactions with a Spearman's Rho correlation coefficient greater than 0.85. The maps were designed so that the dimension of each node is proportional to the number of interconnections a given analyte has. Network maps of SYN− cancer cells included a higher number of interconnections (128) compared

with SYN+ clones (84) (Figure 4). A total of 9 (10%) negative correlations were included in the network of the SYN+ cells compared with 26 (20%) in the SYN− cells. Of interest, the interacting network of SYN+ cancer cells had one main cluster containing a number of cell-cycle regulators. These included the highly interconnected Chk1 S345 along with Cdk2, Cdk4, and Cdk6 (Figure 4A). Phosphorylated Rb, however, was contained in a small network and had low numbers of interactions. The network of the SYN− cells, on the other hand, was more convoluted with a number of clusters. Phosphorylated Rb had a large number of interconnections, while Cdk2, Cdk4, and Cdk6 were scattered between clusters and were poorly interconnected (Figure 4B). Taken together, these data confirm that at the signaling level, SYN+ cancer cells within NSCLCs are characterized by unique interacting signaling networks and molecular profiles compared with SYN− tumor cells.

Molecular profiles of SYN− cells differ based on their proximity to the SYN+ clone

To further dissect heterogeneous behaviors of different clones within the same tissue ecology, for one of the samples, we also captured SYN− tumor cells directly surrounding the
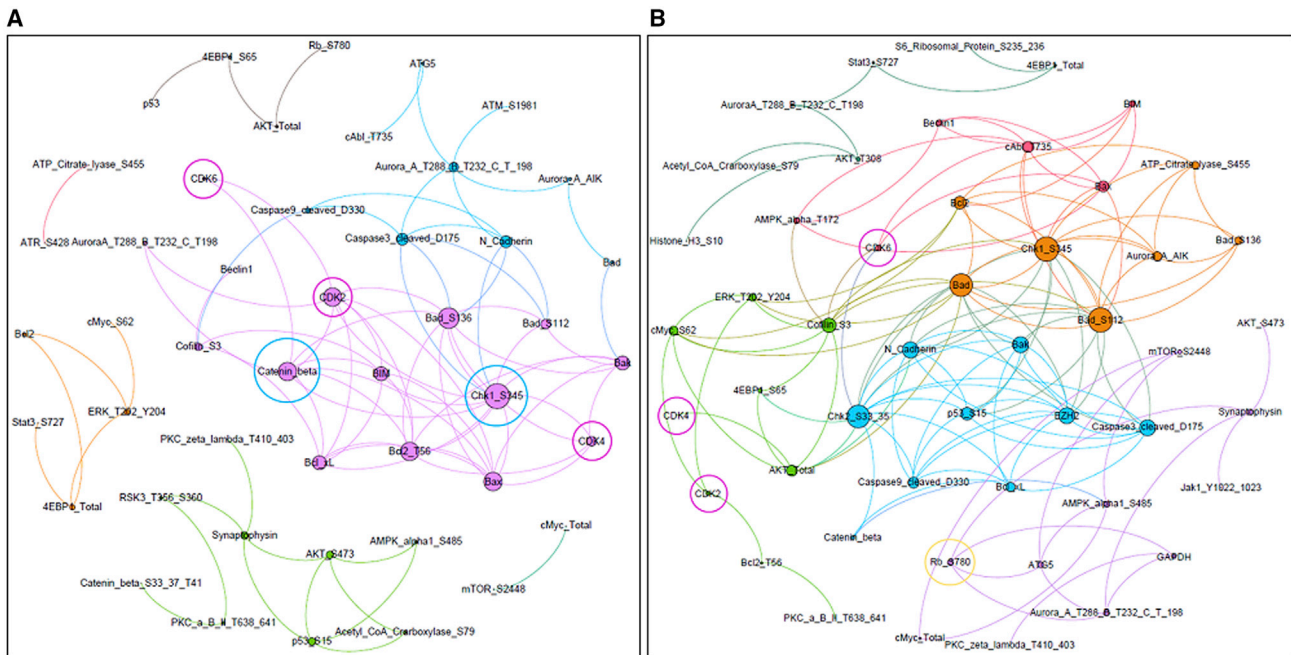
Figure 4. RPPA-based maps capturing paired correlations between signaling proteins in matched SYN+ and SYN− clones isolated via immuno-LCM

(A and B) Correlation maps display proteins with positive or negative Spearman's rank-order correlation coefficients ≥ 0.85; node dimensions are proportional to the number of interconnections of each protein. Correlations in SYN+ and SYN− tumor cells are displayed in (A) and (B), respectively. Pink circles indicate proteins belonging to the Cdk family, blue circles denote cell-cycle regulators, and the yellow circle designates phosphorylated Rb.

SYN+ cancer cells. This proximal population was collected within 100 μm from the SYN+ tumor cells and compared with the other two clones using unsupervised clustering analysis (Figures 3D and S4B). Of interest, SYN+ tumor cells had a higher degree of similarity with the SYN− proximal component compared with the distal clone (Figures 3D and S4B). However, a number of analytes were uniquely elevated in SYN+ tumor cells including phosphorylated Jak1 Y1021/1022, ERK 1/2 T202/Y204, and anti-apoptotic proteins like BAD and Bcl2, as well as unmodified and post-translationally modified Aurora kinases. Rb phosphorylation levels showed a progressive increase from SYN− distal tumor cells to the SYN− proximal tumor cells and SYN+ cells (Figure S4B). In contrast, distal cells had a high expression level of p53 compared with SYN+ and SYN− proximal cells. However, phosphorylation levels of p53 were increased in the proximal and SYN+ clones (Figure S4B). Taken together, these data suggest that key changes known to be associated with NE-TD in cancer like loss of Rb and p53 activities can be detected not only in cells expressing the NE marker SYN+ but also in the nearby SYN− cells. Capturing changes within these two clones may help dissect early events associated with NE-TD in tumors of epithelial origin.

DISCUSSION

In this pilot study, we developed and tested a workflow for isolating NE+ and NE− clones from the complex tissue ecology and generating protein-based signaling profiles. While tissue heterogeneity and the coexistence of different clones play a large role in cancer evolution and response to treatment, finding new ways to dissect and uncover the molecular landscape and behavior of different clones within the tissue microenvironment remains a priority for developing more effective therapeutic approaches. Single-cell technologies have opened new opportunities for capturing molecular events associated with different subpopulations of cells within a complex tumor environment, especially at the DNA and RNA levels. However, the highly heterogeneous nature of tumors, the low abundance of druggable molecules and their level of activation, the varying percentage of NE-like tumor cells in human specimens, and the spatial distribution of NE+ and NE− clones within the tissue ecology make dissecting druggable molecular events uniquely attributable to the NE-TD challenging, even for single-cell technologies (Labib and Kelley, 2020; Lähnemann et al., 2020). Emerging technologies (e.g., CODEX, MIBI) play a prime role in generating detailed cellular profiles and have a higher spatial resolution than the proposed method. However, the workflow proposed presents some advantages and can be complementary to these technologies. First, the immuno-LCM uses a light-microscopy-based system, which remains the elective method in the diagnostic process. Although a number of deep-learning algorithms are under development to implement digital pathology, automated single-cell segmentations remain challenging, especially for underrepresented cell subpopulations (Cui and Zhang, 2021; Baxi et al., 2022; McAlpine et al., 2021). Thus, these systems still need implementation to achieve the accuracy necessary for clinical diagnostics (McAlpine et al., 2021). Second, the RPPA platform has been amply validated in independent

studies, including a number of investigations where it was coupled with sample enrichment via LCM (Mueller et al., 2019; Pierobon et al., 2014; Baldelli et al., 2021). Although individual arrays can only be probed with one antibody targeting a protein of interest, the RPPA can measure hundreds of analytes, including post-translationally modified residues, from a few thousand cells. For example, full signaling profiles have been generated from microdissected core needle biopsies collected in precision medicine clinical trials using a few tissue sections (Wulfkuhle et al., 2018; Wolf et al., 2020; Pierobon et al. 2014, 2022; Jameson et al., 2014). Lastly, because microdissection techniques are a growing component of clinical workflows with assigned CPT codes and the RPPA is currently offered in commercial laboratory as a CLIA/LDT test, the workflow here described has high translational potential and can easily be integrated in future precision medicine efforts. It is known that tumors of epithelial origin utilize a variety of sophisticated mechanisms of resistance to targeted treatments, including the acquisition of NE features and HS to small-cell carcinomas. While historically, the acquisition of SCLC-like characteristics in NSCLCs has been defined as a mechanism of acquired resistance to targeted anti-EGFR treatment, recent findings suggest that this phenomenon has broader implications that may even span beyond response to targeted therapeutics (Bar et al., 2019; Fujita et al., 2016; Quintanal-Villalonga et al., 2021; Rubin et al., 2020; Sehgal et al., 2020). However, because longitudinal sampling after diagnosis is not performed universally, the true incidence and clinical impact of NE-TD and HS in NSCLCs is most likely underestimated and hard to predict.

Roper and colleagues have recently shown that NE-TD in EGFR mutant NSCLCs resistant to Osimertinib can lack HS and suggested that the acquisition of NE markers without morphological changes may precede a full HS to SCLCs in lung cancers of epithelial origin (Roper et al., 2020). Previous studies have also suggested that NE-transformed clones are present at diagnosis in approximately 20% of patients; however, the clinical implications of these cells remain controversial (Feng et al., 2016; Howe et al., 2005; Ionescu et al., 2007; Kriegsmann et al., 2021; Pelosi et al., 2003). Although our analysis is based on a small number of samples and a relatively low number of tumors harboring SYN+ cancer cells (3% and 18% in sets 1 and 2, respectively), NE-like cells were found at the invasive margin of the tumor in 33% of cases, and these tumors were associated with a higher incidence of distance metastases. In addition, 44% of primary tumors containing SYN+ malignant cells had NE-like features also in matched lymph node metastases. Understanding the molecular events that drive NE-TD in lung cancer, even in such early stages, may offer new opportunities for understanding tumor progression, identifying factors within the tumor ecology that may promote NE-TD and HS in response to treatment and devising targeted diagnostic and therapeutic solutions for individual patients.

From a molecular perspective, SYN+ cancer cells were characterized by unique molecular profiles and interactive signaling networks compared with the matched SYN− counterpart (Figures 3 and 4). However, in a previous analysis conducted by our group assessing intratumor heterogeneity of signaling events using an LCM-RPPA-based approach, we detected remarkably

opposed trends (Parasido et al., 2017). Unsupervised clustering analysis of microdissected, but unselected, populations of cancer cells collected from spatially distinct areas within the same tissue section showed a high degree of similarity with almost 70% of matched samples presenting with overlapping molecular characteristics (Parasido et al., 2017). On the contrary, when we used our immuno-LCM workflow to capture SYN+ and SYN− cancer cells, the two components rarely clustered together. Thus, our data suggest that the presence of NE-like cells in the tumor ecology is an important source of intratumor heterogeneity and that sample enrichment is necessary to accurately capture molecular events uniquely attributable to these subpopulations of cancer cells.

A recent work by Quintanal-Villalonga and colleagues has provided a comprehensive multi-omic characterization of the molecular events that are associated with HS to SCLCs in lung adenocarcinomas (Quintanal-Villalonga et al., 2021). Loss of Rb expression measured by IHC was present in all but one of the analyzed samples even in the absence of genomic alterations of the RB1 gene, confirming that genomic-independent events may modulate Rb expression in NE-TD. In line with these findings, we detected a significant deactivation of this tumor suppressor in the SYN+ cancer cells compared with SYN− cells. However, SYN− cells proximal to the NE-like cells showed phosphorylated Rb levels similar to the SYN+ clone. Along with a reduction in Rb activity, all six samples had greater expression of the Rb regulator Cdk6. Four and five samples, respectively, also had increased expression of Cdk2 and Cdk4 in SYN+ cancer cells compared with matched SYN− clones. Taken together, these data suggest that genomic-independent mechanisms may modulate not only Rb expression but also its activation during NE-TD and HS in NSCLCs and that these molecular changes may already be established in early stages of the TD. A recent paper by La Monica and collogues has suggested that phosphorylation of Rb is increased in EGFR mutant NSCLC cell lines that acquire resistance to Osimertinib, regardless of the underlying mechanisms of resistance (La Monica et al., 2020). These preclinical data also suggest that inhibition of the Cdk4/6 axis may modulate response to Osimertinib in NSCLCs, and these findings are currently being evaluated in an ongoing clinical trial (ClinicalTrials.gov: NCT04545710). Validating the role of malfunctioning Cdk/Rb signaling events in NE-like cells and in surrounding SYN− cells may have important diagnostic and therapeutic implications for identifying patients with NSCLC at risk for developing NE-TD and HS or for preventing its occurrence.

With an increasing use of targeted anti-cancer compounds and the development of potent inhibitors designed to overcome on-target resistance, deciphering the molecular mechanisms that drive clonal evolution and resistance to treatment in cancers remains a high priority for advancing precision oncology. Within this paradigm, the immuno-LCM workflow here described may find broad applicability for dissecting spatially intertwined and underrepresented clones (<5% of cells) within complex and heterogeneous cancers and for deciphering molecular mechanisms that provide some clones within the tumor ecology with a fitness advantage and hasty cancer progression. For example, as an expansion of this work, this workflow

can be applied to profile SYN+/− cells in tumors of NE origin like SCLCs or NE tumors. This enrichment method can also be used to isolate and separately profile intertwined clones with different degrees of expression or activation of oncogenes (e.g., HER2 or EGFR), tumor suppressors (e.g., PTEN, p53), or mismatch repair proteins.

Limitations of the study

While this proof-of-concept work highlights the role of immuno-LCM in guiding the isolation of coexisting clones within the heterogeneous molecular landscape of solid tumors, our work is based on a small number of observations with limited statistical power. Thus, drawing decisive conclusions on the biological events that drive NE-TD and potentially HS in NSCLCs is premature. However, the high level of concordance between our findings and previously reported data suggests that the immuno-LCM-based workflow proposed represents a tool for capturing signal-transduction events, drug targets, and downstream substrates across different clones coexisting within a complex cellular system like a tumor. In addition, our approach overcomes the need for a clear spatial separation between different clones within the same tissue, which is required when molecular analyses are coupled with conventional microdissection techniques (Quintanal-Villalonga et al., 2021).

STAR★METHODS

Detailed methods are provided in the online version of this paper and include the following:

- KEY RESOURCES TABLE
- RESOURCE AVAILABILITY
  - Lead contact
  - Materials availability
  - Data and code availability
- EXPERIMENTAL MODEL AND SUBJECT DETAILS
  - Samples collection
- METHOD DETAILS
  - Immunohistochemistry
  - Immuno-laser capture microdissection and protein extraction for RPPA analysis
  - Reverse phase protein microarray construction and immunostaining
- QUANTIFICATION AND STATISTICAL ANALYSIS
  - Image analysis
  - Statistical analysis

SUPPLEMENTAL INFORMATION

Supplemental information can be found online at https://doi.org/10.1016/j.crmeth.2022.100271.

REFERENCES

Arakawa, S., Yoshida, T., Nakayama, Y., Motoi, N., and Ohe, Y. (2020). Small cell cancer transformation of lung adenocarcinoma during durvalumab treatment after chemoradiotherapy. J. Thorac. Oncol. *15*, e145–e146.

Baldelli, E., Haura, E.B., Crinò, L., Cress, D.W., Ludovini, V., Schabath, M.B., Liotta, L.A., Petricoin, E.F., and Pierobon, M. (2015). Impact of upfront cellular enrichment by laser capture microdissection on protein and phosphoprotein drug target signaling activation measurements in human lung cancer: implications for personalized medicine. Proteomics Clin. Appl. *9*, 928–937.

Baldelli, E., Calvert, V., Hodge, A., VanMeter, A., Petricoin, E.F., and Pierobon, M. (2017). Reverse phase protein microarrays. Methods Mol. Biol. *1606*, 149–169.

Baldelli, E., Hodge, K.A., Bellezza, G., Shah, N.J., Gambara, G., Sidoni, A., Mandarano, M., Ruhunusiri, C., Dunetz, B., Abu-Khalaf, M., et al. (2021). PD-L1 quantification across tumor types using the reverse phase protein microarray: implications for precision medicine. J. Immunother Cancer *9*, e002179.

Bar, J., Ofek, E., Barshack, I., Gottfried, T., Zadok, O., Kamer, I., Urban, D., Perelman, M., and Onn, A. (2019). Transformation to small cell lung cancer as a mechanism of resistance to immunotherapy in non-small cell lung cancer. Lung Cancer *138*, 109–115.

Baxi, V., Edwards, R., Montalto, M., and Saha, S. (2022). Digital pathology and artificial intelligence in translational medicine and clinical practice. Mod. Pathol. *35*, 23–32.

Buckanovich, R.J., Sasaroli, D., O'brien-Jenkins, A., Botbyl, J., Conejo-Garcia, J.R., Benencia, F., Liotta, L.A., Gimotty, P.A., and Coukos, G. (2006). Use of immuno-LCM to identify the in situ expression profile of cellular constituents of the tumor microenvironment. Cancer Biol. Ther. *5*, 635–642.

Chabrat, A., Doucet-Beaupré, H., and Lévesque, M. (2015). RNA isolation from cell specific subpopulations using laser-capture microdissection combined with rapid immunolabeling. J. Vis. Exp. https://doi.org/10.3791/52510.

Chai, J.T., Ruparelia, N., Goel, A., Kyriakou, T., Biasiolli, L., Edgar, L., Handa, A., Farrall, M., Watkins, H., and Choudhury, R.P. (2018). Differential gene expression in macrophages from human atherosclerotic plaques shows convergence on pathways implicated by genome-wide association study risk variants. Arterioscler. Thromb. Vasc. Biol. *38*, 2718–2730.

Chiechi, A., Novello, C., Magagnoli, G., Petricoin, E.F., Deng, J., Benassi, M.S., Picci, P., Vaisman, I., Espina, V., and Liotta, L.A. (2013). Elevated TNFR1 and serotonin in bone metastasis are correlated with poor survival following bone metastasis diagnosis for both carcinoma and sarcoma primary tumors. Clin. Cancer Res. *19*, 2473–2485.

Crea, F., Venalainen, E., Ci, X., Cheng, H., Pikor, L., Parolia, A., Xue, H., Nur Saidy, N.R., Lin, D., Lam, W., et al. (2016). The role of epigenetics and long non-coding RNA MIAT in neuroendocrine prostate cancer. Epigenomics *8*, 721–731.

Cui, M., and Zhang, D.Y. (2021). Artificial intelligence and computational pathology. Lab. Invest. *101*, 412–422.

Demarest, T.G., Murugesan, N., Shrestha, B., and Pachter, J.S. (2012). Rapid expression profiling of brain microvascular endothelial cells by immuno-laser capture microdissection coupled to TaqMan(®) low density array. J. Neurosci. Methods *206*, 200–204.

Espina, V., Wulfkuhle, J.D., Calvert, V.S., VanMeter, A., Zhou, W., Coukos, G., Geho, D.H., Petricoin, E.F., and Liotta, L.A. (2006). Laser-capture microdissection. Nat. Protoc. *1*, 586–603.

Espina, V., Heiby, M., Pierobon, M., and Liotta, L.A. (2007). Laser capture microdissection technology. Expert Rev. Mol. Diagn *7*, 647–657.

Farrell, A.S., Joly, M.M., Allen-Petersen, B.L., Worth, P.J., Lanciault, C., Sauer, D., Link, J., Pelz, C., Heiser, L.M., Morton, J.P., et al. (2017). MYC regulates ductal-neuroendocrine lineage plasticity in pancreatic ductal adenocarcinoma associated with poor outcome and chemoresistance. Nat. Commun. *8*, 1728.

Fend, F., Emmert-Buck, M.R., Chuaqui, R., Cole, K., Lee, J., Liotta, L.A., and Raffeld, M. (1999). Immuno-LCM: laser capture microdissection of immunostained frozen sections for mRNA analysis. Am. J. Pathol. *154*, 61–66.

Feng, J., Sheng, H., Zhu, C., Qian, X., Wan, D., Su, D., Chen, X., and Zhu, L. (2016). Correlation of neuroendocrine features with prognosis of non-small cell lung cancer. Oncotarget *7*, 71727–71736.

Fujita, S., Masago, K., Katakami, N., and Yatabe, Y. (2016). Transformation to SCLC after treatment with the ALK inhibitor alectinib. J. Thorac. Oncol. *11*, e67–e72.

Gallagher, R.I., and Espina, V. (2014). Reverse phase protein arrays: mapping the path towards personalized medicine. Mol. Diagn. Ther. *18*, 619–630.

Howe, M.C., Chapman, A., Kerr, K., Dougal, M., Anderson, H., and Hasleton, P.S. (2005). Neuroendocrine differentiation in non-small cell lung cancer and its relation to prognosis and therapy. Histopathology *46*, 195–201.

Hunt, A.L., Pierobon, M., Baldelli, E., Oliver, J., Mitchell, D., Gist, G., Bateman, N.W., Larry Maxwell, G., Petricoin, E.F., and Conrads, T.P. (2020). The impact of ultraviolet- and infrared-based laser microdissection technology on phosphoprotein detection in the laser microdissection-reverse phase protein array workflow. Clin. Proteomics *17*, 9.

Ionescu, D.N., Treaba, D., Gilks, C.B., Leung, S., Renouf, D., Laskin, J., Wood-Baker, R., and Gown, A.M. (2007). Nonsmall cell lung carcinoma with neuroendocrine differentiation–an entity of no clinical or prognostic significance. Am. J. Surg. Pathol. *31*, 26–32.

Jameson, G.S., Petricoin, E.F., Sachdev, J., Liotta, L.A., Loesch, D.M., Anthony, S.P., Chadha, M.K., Wulfkuhle, J.D., Gallagher, R.I., Reeder, K.A., et al. (2014). A pilot study utilizing multi-omic molecular profiling to find potential targets and select individualized treatments for patients with previously treated metastatic breast cancer. Breast Cancer Res. Treat. *147*, 579–588.

Kleist, B., and Poetsch, M. (2015). Neuroendocrine differentiation: the mysterious fellow of colorectal cancer. World J. Gastroenterol. *21*, 11740–11747.

Kriegsmann, K., Zgorzelski, C., Kazdal, D., Cremer, M., Muley, T., Winter, H., Longuespée, R., Kriegsmann, J., Warth, A., and Kriegsmann, M. (2020). Insulinoma-associated protein 1 (INSM1) in thoracic tumors is less sensitive but more specific compared with synaptophysin, Chromogranin A, and CD56. Appl. Immunohistochem. Mol. Morphol. *28*, 237–242.

Kriegsmann, K., Zgorzelski, C., Muley, T., Christopoulos, P., Thomas, M., Winter, H., Eichhorn, M., Eichhorn, F., von Winterfeld, M., Herpel, E., et al. (2021). Role of Synaptophysin, Chromogranin and CD56 in adenocarcinoma and squamous cell carcinoma of the lung lacking morphological features of neuroendocrine differentiation: a retrospective large-scale study on 1170 tissue samples. BMC Cancer *21*, 486.

La Monica, S., Fumarola, C., Cretella, D., Bonelli, M., Minari, R., Cavazzoni, A., Digiacomo, G., Galetti, M., Volta, F., Mancini, M., et al. (2020). Efficacy of the CDK4/6 dual inhibitor abemaciclib in EGFR-mutated NSCLC cell lines with different resistance mechanisms to Osimertinib. Cancers *13*, E6.

Labib, M., and Kelley, S., O. (2020). Single- cell analysis targeting the proteome. Nat. Rev. Chem *4*, 143–158.

Lähnemann, D., Köster, J., Szczurek, E., McCarthy, D.J., Hicks, S.C., Robinson, M.D., Vallejos, C.A., Campbell, K.R., Beerenwinkel, N., Mahfouz, A., et al. (2020). Eleven grand challenges in single-cell data science. Genome Biol. *21*, 31.

Lee, J.-K., Lee, J., Kim, S., Kim, S., Youk, J., Park, S., An, Y., Keam, B., Kim, D.-W., Heo, D.S., et al. (2017). Clonal history and genetic predictors of transformation into small-cell carcinomas from lung adenocarcinomas. J. Clin. Oncol. *35*, 3065–3074.

Liotta, L.A., Pappalardo, P.A., Carpino, A., Haymond, A., Howard, M., Espina, V., Wulfkuhle, J., and Petricoin, E. (2021). Laser Capture Proteomics: spatial tissue molecular profiling from the bench to personalized medicine. Expert Rev. Proteomics *18*, 845–861.

Liu, Y., Wu, J., Yan, G., Hou, R., Zhuang, D., Chen, L., Pang, Q., and Zhu, J. (2010). Proteomic analysis of prolactinoma cells by immuno-laser capture microdissection combined with online two-dimensional nano-scale liquid chromatography/mass spectrometry. Proteome Sci. *8*, 2.

Macdonald, J.A., Murugesan, N., and Pachter, J.S. (2008). Validation of immuno-laser capture microdissection coupled with quantitative RT-PCR to probe blood-brain barrier gene expression in situ. J. Neurosci. Methods *174*, 219–226.

Marcoux, N., Gettinger, S.N., O'Kane, G., Arbour, K.C., Neal, J.W., Husain, H., Evans, T.L., Brahmer, J.R., Muzikansky, A., Bonomi, P.D., et al. (2018). EGFR-mutant adenocarcinomas that transform to small-cell lung cancer and other neuroendocrine carcinomas: clinical outcomes. J. Clin. Orthod. *37*, 278–285.

McAlpine, E.D., Pantanowitz, L., and Michelow, P.M. (2021). Challenges developing deep learning algorithms in cytology. Acta Cytol. *65*, 301–309.

Miura, N., Matsubara, T., Takamori, S., Haratake, N., Toyozawa, R., Yamaguchi, M., Seto, T., Taguchi, K., and Takenoyama, M. (2020). Histological conversion from adenocarcinoma to small cell carcinoma of the lung after treatment with an immune checkpoint inhibitor: a case report. Oxf. Med. Case Reports *2020*, omaa026.

Mueller, C., Davis, J.B., and Liotta, L.A. (2019). Combining the "sibling technologies" of laser capture microdissection and reverse phase protein microarrays. Adv. Exp. Med. Biol. *1188*, 95–111.

Niederst, M.J., Sequist, L.V., Poirier, J.T., Mermel, C.H., Lockerman, E.L., Garcia, A.R., Katayama, R., Costa, C., Ross, K.N., Moran, T., et al. (2015). RB loss in resistant EGFR mutant lung adenocarcinomas that transform to small-cell lung cancer. Nat. Commun. *6*, 6377.

Nyquist, M.D., Corella, A., Coleman, I., De Sarkar, N., Kaipainen, A., Ha, G., Gulati, R., Ang, L., Chatterjee, P., Lucas, J., et al. (2020). Combined TP53 and RB1 loss promotes prostate cancer resistance to a spectrum of therapeutics and confers vulnerability to replication stress. Cell Rep. *31*, 107669.

Offin, M., Chan, J.M., Tenet, M., Rizvi, H.A., Shen, R., Riely, G.J., Rekhtman, N., Daneshbod, Y., Quintanal-Villalonga, A., Penson, A., et al. (2019). Concurrent RB1 and TP53 alterations define a subset of EGFR-Mutant lung cancers at risk for histologic transformation and inferior clinical, outcomes. J. Thorac. Oncol. *14*, 1784–1793.

Oser, M.G., Niederst, M.J., Sequist, L.V., and Engelman, J.A. (2015). Transformation from non-small-cell lung cancer to small-cell lung cancer: molecular drivers and cells of origin. Lancet Oncol. *16*, e165–e172.

Ostano, P., Mello-Grand, M., Sesia, D., Gregnanin, I., Peraldo-Neia, C., Guana, F., Jachetti, E., Farsetti, A., and Chiorino, G. (2020). Gene expression signature predictive of neuroendocrine transformation in prostate adenocarcinoma. Int. J. Mol. Sci. *21*.

Parasido, E.M., Silvestri, A., Canzonieri, V., Belluco, C., Diodoro, M.G., Milione, M., Melotti, F., De Maria, R., Liotta, L., Petricoin, E.F., et al. (2017). Protein drug target activation homogeneity in the face of intra-tumor heterogeneity: implications for precision medicine. Oncotarget *8*, 48534–48544.

Patel, G.K., Chugh, N., and Tripathi, M. (2019). Neuroendocrine differentiation of prostate cancer-an intriguing example of tumor evolution at play. Cancers *11*.

Pelosi, G., Pasini, F., Sonzogni, A., Maffini, F., Maisonneuve, P., Iannucci, A., Terzi, A., De Manzoni, G., Bresaola, E., and Viale, G. (2003). Prognostic

implications of neuroendocrine differentiation and hormone production in patients with Stage I nonsmall cell lung carcinoma. Cancer 97, 2487–2497.

Pierobon, M., Silvestri, A., Spira, A., Reeder, A., Pin, E., Banks, S., Parasido, E., Edmiston, K., Liotta, L., and Petricoin, E. (2014). Pilot phase I/II personalized therapy trial for metastatic colorectal cancer: evaluating the feasibility of protein pathway activation mapping for stratifying patients to therapy with imatinib and panitumumab. J. Proteome Res. 13, 2846–2855.

Pierobon, M., Robert, N.J., Northfelt, D.W., Jahanzeb, M., Wong, S., Hodge, K.A., Baldelli, E., Aldrich, J., Craig, D.W., Liotta, L.A., et al. (2022). Multiomic molecular profiling guide's efficacious treatment selection in refractory metastatic breast cancer: a prospective phase II clinical trial. Mol. Oncol. 16, 104–115.

Pin, E., Federici, G., and Petricoin, E.F. (2014). Preparation and use of reverse protein microarrays. Curr. Protoc. Protein Sci. 75, 27.7.1–27.7.29.

Quintanal-Villalonga, Á., Chan, J.M., Yu, H.A., Pe'er, D., Sawyers, C.L., Sen, T., and Rudin, C.M. (2020). Lineage plasticity in cancer: a shared pathway of therapeutic resistance. Nat. Rev. Clin. Oncol. 17, 360–371.

Quintanal-Villalonga, A., Taniguchi, H., Zhan, Y.A., Hasan, M.M., Chavan, S.S., Meng, F., Uddin, F., Manoj, P., Donoghue, M.T.A., Won, H.H., et al. (2021). Multi-omic analysis of lung tumors defines pathways activated in neuroendocrine transformation. Cancer Discov. Candisc. 1863, 2021.

Rajaram, S., Roth, M.A., Malato, J., VandenBerg, S., Hann, B., Atreya, C.E., Altschuler, S.J., and Wu, L.F. (2019). A multi-modal data resource for investigating topographic heterogeneity in patient-derived xenograft tumors. Sci. Data 6, 253.

Ramnarine, V.R., Kobelev, M., Gibb, E.A., Nouri, M., Lin, D., Wang, Y., Buttyan, R., Davicioni, E., Zoubeidi, A., and Collins, C.C. (2019). The evolution of long noncoding RNA acceptance in prostate cancer initiation, progression, and its clinical utility in disease management. Eur. Urol. 76, 546–559.

Rapkiewicz, A., Espina, V., Zujewski, J.A., Lebowitz, P.F., Filie, A., Wulfkuhle, J., Camphausen, K., Petricoin, E.F., Liotta, L.A., and Abati, A. (2007). The needle in the haystack: application of breast fine-needle aspirate samples to quantitative protein microarray technology. Cancer 111, 173–184.

Roper, N., Brown, A.-L., Wei, J.S., Pack, S., Trindade, C., Kim, C., Restifo, O., Gao, S., Sindiri, S., Mehrabadi, F., et al. (2020). Clonal evolution and heterogeneity of Osimertinib acquired resistance mechanisms in EGFR mutant lung cancer. Cell Rep. Med. 1.

Rubin, M.A., Bristow, R.G., Thienger, P.D., Dive, C., and Imielinski, M. (2020). Impact of lineage plasticity to and from a neuroendocrine phenotype on progression and response in prostate and lung cancers. Mol. Cell 80, 562–577.

Rupp, C., Dolznig, H., Puri, C., Schweifer, N., Sommergruber, W., Kraut, N., Rettig, W.J., Kerjaschki, D., and Garin-Chesa, P. (2006). Laser capture microdissection of epithelial cancers guided by antibodies against fibroblast activation protein and endosialin. Diagn. Mol. Pathol. 15, 35–42.

Sehgal, K., Varkaris, A., Viray, H., VanderLaan, P.A., Rangachari, D., and Costa, D.B. (2020). Small cell transformation of non-small cell lung cancer on immune checkpoint inhibitors: uncommon or under-recognized? J Immunother Cancer 8.

Sekkate, S., Ladrat, L., Pouliquen, C., Callens, C., Geay, J.F., and Beuzeboc, P. (2021). Neuroendocrine differentiation in metastatic breast cancer following CDK 4/6 inhibitors. J. Clin. Oncol. 39, e1302.

Shaurova, T., Zhang, L., Goodrich, D.W., and Hershberger, P.A. (2020). Understanding lineage plasticity as a path to targeted therapy failure in EGFR-mutant non-small cell lung cancer. Front. Genet. 11, 281.

Sherr, C.J., and McCormick, F. (2002). The RB and p53 pathways in cancer. Cancer Cell 2, 103–112.

Shia, J., Tickoo, S.K., Guillem, J.G., Qin, J., Nissan, A., Hoos, A., Stojadinovic, A., Ruo, L., Wong, W.D., Paty, P.B., et al. (2002). Increased endocrine cells in treated rectal adenocarcinomas: a possible reflection of endocrine differentiation in tumor cells induced by chemotherapy and radiotherapy. Am. J. Surg. Pathol. 26, 863–872.

Signore, M., Manganelli, V., and Hodge, A. (2017). Antibody validation by western blotting. Methods Mol. Biol. 1606, 51–70.

Simpson, J.E., Wharton, S.B., and Heath, P.R. (2018). Immuno-laser-capture microdissection for the isolation of enriched glial populations from frozen post-mortem human brain. Methods Mol. Biol. 1723, 273–284.

Tagliafierro, L., Bonawitz, K., Glenn, O.C., and Chiba-Falek, O. (2016). Gene expression analysis of neurons and astrocytes isolated by laser capture microdissection from frozen human brain tissues. Front. Mol. Neurosci. 9, 72.

Tangrea, M.A., Hanson, J.C., Bonner, R.F., Pohida, T.J., Rodriguez-Canales, J., and Emmert-Buck, M.R. (2011). Immunoguided microdissection techniques. Methods Mol. Biol. 755, 57–66.

Tiwari, R., Manzar, N., and Ateeq, B. (2020). Dynamics of cellular plasticity in prostate cancer progression. Front. Mol. Biosci. 7, 130.

Travis, W., Beasley, M., Papotti, M., Rekhtman, N., and Rossi, G. (2021). WHO Classification of Tumours Editorial Board. Thoracic Tumours (International Agency for Research on Cancer).

Vlachostergios, P.J., and Papandreou, C.N. (2015). Targeting neuroendocrine prostate cancer: molecular and clinical perspectives. Front. Oncol. 5, 6.

Wang, M., Abi-Raad, R., Baldassarri, R., Adeniran, A.J., and Cai, G. (2021). Expression of insulinoma-associated protein 1 in non-small cell lung cancers: a diagnostic pitfall for neuroendocrine tumors. Hum. Pathol. 115, 104–111.

Wolf, D.M., Yau, C., Wulfkuhle, J., Brown-Swigart, L., Gallagher, R.I., Magbanua, M.J.M., O'Grady, N., Hirst, G., I-SPY 2 TRIAL Investigators; and Asare, S., et al. (2020). Mechanism of action biomarkers predicting response to AKT inhibition in the I-SPY 2 breast cancer trial. NPJ Breast Cancer 6, 48.

Worsley, C.M., Mayne, E.S., and Veale, R.B. (2016). Clone wars: the evolution of therapeutic resistance in cancer. Evol. Med. Public Health 2016, 180–181.

Wulfkuhle, J.D., Yau, C., Wolf, D.M., Vis, D.J., Gallagher, R.I., Brown-Swigart, L., Hirst, G., Voest, E.E., DeMichele, A., Hylton, N., et al. (2018). Evaluation of the HER/PI3K/AKT family signaling network as a predictive biomarker of pathologic complete response for patients with breast cancer treated with neratinib in the I-SPY 2 TRIAL. JCO Precis Oncol. 2, PO.18.00024.

Yatabe, Y., Dacic, S., Borczuk, A.C., Warth, A., Russell, P.A., Lantuejoul, S., Beasley, M.B., Thunnissen, E., Pelosi, G., Rekhtman, N., et al. (2019). Best practices recommendations for diagnostic immunohistochemistry in lung cancer. J. Thorac. Oncol. 14, 377–407.

CellPress
OPEN ACCESS

STAR★METHODS

KEY RESOURCES TABLE

REAGENT or RESOURCE	SOURCE	IDENTIFIER
Antibodies		
Rabbit polyclonal anti-4E-BP1	Cell Signaling Technology	Cat# 9452; RRID: AB_331692
Rabbit polyclonal anti-phospho-4E-BP1 (S65)	Cell Signaling Technology	Cat# 9451; RRID: AB_330947
Rabbit polyclonal anti-phospho-Acetyl-CoA Carboxylase (S79)	Cell Signaling Technology	Cat# 3661; RRID: AB_330337
Rabbit polyclonal anti-Akt	Cell Signaling Technology	Cat# 9272; RRID: AB_329827
Rabbit polyclonal anti-phospho-AKT (S473) XP	Cell Signaling Technology	Cat# 4060; RRID: AB_2315049
Rabbit polyclonal anti-phospho-AKT (T308)	Cell Signaling Technology	Cat# 9275; RRID: AB_329828
Rabbit monoclonal anti-phospho-AMPKalpha (T172) (D79.5E)	Cell Signaling Technology	Cat# 4188; RRID: AB_2169396
Rabbit polyclonal anti—phospho-AMPKalpha1 (S485)	Cell Signaling Technology	Cat# 4184; RRID: AB_390759
Rabbit polyclonal anti-ATG5	Cell Signaling Technology	Cat# 2630; RRID: AB_2062340
Rabbit monoclonal anti-phospho-ATM (S1981) (D6H9)	Cell Signaling Technology	Cat# 5883; RRID: AB_10835213
Rabbit polyclonal anti-phospho-ATP-Citrate Lyase (S455)	Cell Signaling Technology	Cat# 4331; RRID: AB_2257987
Rabbit polyclonal anti—phospho-ATR (S428)	Cell Signaling Technology	Cat# 2853; RRID: AB_2290281
Rabbit monoclonal anti-Aurora A (T288)/B (T232)/C (T198) (Clone D13A11)	Cell Signaling Technology	Cat# 2914; RRID: AB_2061631
Rabbit polyclonal anti-Aurora A/AIK	Cell Signaling Technology	Cat# 3092; RRID: AB_2061342
Rabbit polyclonal anti-Bad	Cell Signaling Technology	Cat# 9292; RRID: AB_331419
Rabbit polyclonal anti-phospho-BAD (S112)	Cell Signaling Technology	Cat# 9291; RRID: AB_331417
Rabbit polyclonal anti-phospho-BAD (S136)	Cell Signaling Technology	Cat# 9295; RRID: AB_2258874
Rabbit monoclonal anti-Bak (D4E4)	Cell Signaling Technology	Cat# 12105; RRID: AB_2716685
Rabbit polyclonal anti-Bax	Cell Signaling Technology	Cat# 2772; RRID: AB_10695870
Rabbit polyclonal anti-Bcl-2	Cell Signaling Technology	Cat# 2872; RRID: AB_10693462
Rabbit polyclonal anti-phospho-Bcl-2 (T56)	Cell Signaling Technology	Cat# 2875; RRID: AB_2243462
Rabbit polyclonal anti-Bcl-xL	Cell Signaling Technology	Cat# 2762; RRID: AB_10694844
Rabbit polyclonal anti-Beclin 1	Cell Signaling Technology	Cat# 3738; RRID: AB_490837
Rabbit polyclonal anti-BIM	Cell Signaling Technology	Cat# 2933; RRID: AB_1030947
Rabbit polyclonal anti-phospho-c-Abl (T735)	Cell Signaling Technology	Cat# 2864; RRID: AB_331066
Rabbit polyclonal anti-Caspase-3, cleaved (D175)	Cell Signaling Technology	Cat# 9661; RRID: AB_2341188
Rabbit polyclonal anti-Caspase-9, cleaved (D330)	Cell Signaling Technology	Cat# 9501; RRID: AB_331424
Rabbit polyclonal anti-Catenin (beta)	Cell Signaling Technology	Cat# 9562; RRID: AB_331149
Rabbit polyclonal anti-CDK2 (clone 78B2)	Cell Signaling Technology	Cat# 2546; RRID: AB_2276129
Rabbit monoclonal anti-CDK4 (clone D9G3E)	Cell Signaling Technology	Cat# 12790; RRID: AB_2631166
Rabbit monoclonal anti-CDK6 (D4S8S)	Cell Signaling Technology	Cat# 13331; RRID: AB_2721897

(Continued on next page)

Continued

REAGENT or RESOURCE	SOURCE	IDENTIFIER
Rabbit polyclonal anti-phospho-Chk-1 (S345)	Cell Signaling Technology	Cat# 2341; RRID: AB_330023
Rabbit polyclonal anti-phospho-Chk-2 (S33/35)	Cell Signaling Technology	Cat# 2665; RRID: AB_10831817
Rabbit polyclonal anti-c-Myc	Cell Signaling Technology	Cat# 9402; RRID: AB_2151827
Rabbit monoclonal anti-phospho-c-Myc (S62) (E1J4K)	Cell Signaling Technology	Cat# 13748; RRID: AB_2687518
Rabbit monoclonal anti-phospho-Cofilin (S3) (clone 77G2)	Cell Signaling Technology	Cat# 3313; RRID: AB_2080597
Rabbit polyclonal anti-phospho-Cyclin D1 (T286) XP	Cell Signaling Technology	Cat# 3300; RRID: AB_2070561
Rabbit monoclonal anti-Cyclin D2 (clone D52F9)	Cell Signaling Technology	Cat# 3741; RRID: AB_2070685
Rabbit polyclonal anti-phospho-ERK (T202/Y204)	Cell Signaling Technology	Cat# 9101; RRID: AB_331646
Rabbit polyclonal anti-EZH2	Cell Signaling Technology	Cat# 5246; RRID: AB_10694683
Rabbit polyclonal anti-phospho-GSK-3beta (S9)	Cell Signaling Technology	Cat# 9336; RRID: AB_331405
Rabbit polyclonal anti-phospho-Histone H3 (S10) Mitosis Marker	Upstate	Cat# 06-570; RRID: AB_310177
Rabbit polyclonal anti-phospho-Jak1 (Y1022/1023)	Cell Signaling Technology	Cat# 3331; RRID: AB_2265057
Rabbit polyclonal anti-phospho-mTOR (S2448)	Cell Signaling Technology	Cat# 2971; RRID: AB_330970
Rabbit polyclonal anti-N-Cadherin	Cell Signaling Technology	Cat# 4061; RRID: AB_10694647
Rabbit polyclonal anti-phospho-NF-kappaB p65 (S536)	Cell Signaling Technology	Cat# 3031; RRID: AB_330559
Rabbit polyclonal anti-p53	Cell Signaling Technology	Cat# 9282; RRID: AB_331476
Rabbit polyclonal anti-phospho-p53 (S15)	Cell Signaling Technology	Cat# 9284; RRID: AB_331464
Rabbit polyclonal anti-PD-L1 (28-8)	Abcam	Cat# ab205921; RRID: AB_2687878
Rabbit polyclonal anti-phospho-PKC a/BII (T638/641)	Cell Signaling Technology	Cat# 9375; RRID: AB_2284224
Rabbit polyclonal anti-phospho-PKC zeta/lambda (T410/403)	Cell Signaling Technology	Cat# 9378; RRID: AB_2168217
Rabbit polyclonal anti-phospho-Rb (S780)	Cell Signaling Technology	Cat# 3590; RRID: AB_2177182
Rabbit polyclonal anti-phospho-RSK3 (T356/S360)	Cell Signaling Technology	Cat# 9348; RRID: AB_390805
Rabbit polyclonal anti-phospho-S6 Ribosomal Protein (S235/236) (2F9)	Cell Signaling Technology	Cat# 4856; RRID: AB_2181037
Rat monoclonal anti-Snail (SN9H2)	Cell Signaling Technology	Cat# 4719; RRID: AB_2191760
Rabbit polyclonal anti-phospho-Stat3 (S727)	Cell Signaling Technology	Cat# 9134; RRID: AB_331589
Rabbit monoclonal anti-Synaptophysin (clone D8F6H)	Cell Signaling Technology	Cat# 36406; RRID: AB_2799098
Mouse monoclonal anti-Synaptophysin (clone 27G12)	Leica Biosystems	Cat# NCL-L-SYNAP-299; RRID: AB_442136
Mouse monoclonal anti-Synaptophysin (clone 27G12)	Biocare Medical	Cat# CM371AK; RRID: AB_10581027
Goat Anti-Rabbit IgG Antibody (HL), Biotinylated	Vector Laboratories	Cat# BA-1000-1.5; RRID: AB_2313606

(Continued on next page)

Continued

REAGENT or RESOURCE	SOURCE	IDENTIFIER
Biological samples		
Primary tumors (n = 50) with 23 matched lymph node metastases collected from NSCLC patients undergoing surgical procedures	Santa Maria della Misericordia Hospital, Perugia, Italy	N/A
Retrospective samples (n = 188) collected from NSCLC patients	Santa Maria della Misericordia Hospital, Perugia, Italy	N/A
Chemicals, peptides, and recombinant proteins		
Xylene	Sigma-Aldrich	Cat# 247642-4L-CB
Ethanol	Sigma-Aldrich	Cat# E7023-500ML
β-mercaptoethanol	Fisher Scientific	Cat# BP176-100
Sypro Ruby Protein Blot Stain	Invitrogen	Cat# S11791
Methanol	Fisher Scientific	Cat# A412-1
Acetic acid	Fisher Scientific	Cat# A38-212
Reblot Plus Mild Antibody stripping solution	Millipore	Cat# 2502
PBS	GIBCO	Cat# 14190-136
I-block	Invitrogen	Cat# T2015
IRDye680 dye	LI-COR Biosciences	Cat# 926-68079
Critical commercial assays		
Bond™ Polymer Refine Detection system	Leica Biosystems	Cat# DS9800
Diva Decloaker buffer	Biocare Medical	Cat# DV2004LX
MACH 2 Mouse HRP-Polymer Detection kit	Biocare Medical	Cat# MHRP520G
QProteome FFPE Tissue kit	Qiagen	Cat# 37623
GenPoint kit	Agilent	Cat# K0620
Deposited data		
Reverse phase protein array (RPPA)	This paper	Zenodo: https://doi.org/10.5281/zenodo.6857765
Software and algorithms		
Micro-Vigene	VigeneTech, Inc.	http://www.vigenetech.com/MicroVigene.htm
JMP v16	SAS Institute Inc.	https://www.jmp.com/en_us/software/data-analysis-software.html
GraphPad Prism v. 9.3.0	GraphPad Software	https://www.graphpad.com/scientific-software/prism/
Gephi v0.9.2	Chiechi et al., 2013	https://gephi.org/
Other		
Macro LCM caps	Arcturus Bioscience	Cat# LCM0212
Nitrocellulose-coated glass slides (ONCYTE AVID 1- 22mm × 51mm NC Pad Per Slide Glass, 25 × 75 × 1mm, Small Dark Blue Box)	Grace Bio-labs	Cat# RD478691-M

RESOURCE AVAILABILITY

Lead contact
Further information and requests for resources and reagents should be directed to and will be fulfilled by the lead contact, Mariaelena Pierobon (mpierobo@gmu.edu).

Materials availability
This study did not generate new unique reagents.

Data and code availability

EXPERIMENTAL MODEL AND SUBJECT DETAILS

Samples collection

A total of 238 samples collected from NSCLC patients treated at the Santa Maria della Misericordia Hospital, Perugia, Italy, were screened to identify samples containing SYN+ cancerous cells. Samples were collected under voluntary informed consent and processed for molecular analyses according to IRB approval collected by the enrolling institution. To preserve the diagnostic process and maximize tissue usage, only cases with abundant left-over tissues after standard diagnostic evaluation were used. The whole dataset included two independent sets of samples. Set 1 included 50 primary tumors with 23 matched lymph node metastases that were collected from NSCLC patients undergoing surgical procedures at the enrolling institution. Set 2 was comprised of 188 retrospective samples collected from NSCLC patients. Biospecimens had previously been processed and included on a tissue microarray (TMA). Samples were spread across 18 slides and an average of four 2 mm-cores were analyzed for each sample, with four exceptions where only 2 cores were included.

METHOD DETAILS

Immunohistochemistry

SYN expression data were collected across the two datasets by the enrolling institution using an IHC diagnostic protocol. SYN was selected as a marker of NE features for the following reasons: A) higher specificity for NE differentiation that can be missed by the CD56 marker (Pelosi et al., 2003; Yatabe et al., 2019); B) SYN diffuse cytoplasmic stain in NE-tumor cells is less prone to misinterpretation compared, for example, to weak, focal, and cytoplasmic faintly granular Chromogranin A stain in high grade neuroendocrine tumors (Pelosi et al., 2003), C) SYN is usually expressed in less differentiated NE lung tumors compared to Chromogranin A (Pelosi et al., 2003), and D) SYN has greater specificity and sensitivity than the Insulinoma-associated Protein 1 (INSM1) in NSCLC, especially in squamous cell carcinomas and large cell neuroendocrine tumors. Indeed, recent findings have suggested that INSM1 is a reliable biomarker of differentiation in SCLCs. However, it should be used in conjunction with other NE markers in NSCLCs (Wang et al., 2021; Kriegsmann et al., 2020). IHC was performed on FFPE archived tissues samples and TMA using the BOND-III fully automated IHC stainer (Leica Biosystems, Nußloch, Germany). Antigen retrieval was performed using heat induced epitope retrieval at pH = 6 for 30 min, followed by incubation with a primary anti-Synaptophysin antibody (clone 27G12) (Ready-to-Use; mouse; Leica Biosystems, Newcastle, UK). Signal detection was performed using the commercially available kit Bond™ Polymer Refine Detection system (Leica Biosystems, Newcastle, UK) following manufacturer's instructions. Samples were analyzed by two certified pathologists (MM and GB), evaluating both the immunolabel intensity levels (assessed as 0: absent; 1: mild; 2: moderate; 3: intense) and the percentage of immunostained tumor cells.

Immuno-laser capture microdissection and protein extraction for RPPA analysis

FFPE tissues were sectioned at 4 μm and mounted on electrostatically charged glass slides. The morning of the LCM, before immunostaining, slides were deparaffinized in xylene for 30 min, rehydrated in 100%, 90%, 70% ethanol and washed in water. Heat-Induced Epitope Retrieval was performed using the Diva Decloaker buffer (Biocare Medical, Pacheco, CA, USA) in a water bath at 98°C for one hour. Slides were then rinsed twice with water followed by IHC staining using an automated system (Dako Cytomation, Carpinteria, CA, USA). Briefly, tissue sections were probed for 30 min with a mouse anti-SYN antibody (Dil 1:50; mouse; Biocare Medical, Pacheco, CA, USA). The MACH 2 Mouse HRP-Polymer Detection kit (Biocare Medical, Pacheco, CA, USA) was used as a one-step polymer detection system. Following IHC the slides were dehydrated in ethanol (70%, 95% and 100%) and xylene (Tangrea et al., 2011). Deparaffinization and hydration steps required for the IHC analysis match the steps that are conventionally used when FFPE samples are microdissected. To minimize the impact of the IHC staining on downstream RPPA analysis, a short heat-induced antigen retrieval process (1 h in a water bath at 98°C) was used to avoid prolonged overnight incubations, limit the effect of the antigen retrieval on antigens and antibody structures, and preserve epitopes for downstream analysis by RPPA. Using a Pixcell II LCM system (Arcturus Bioscience, Mountain View, CA, USA) equipped with an infrared laser, SYN+ and SYN- malignant cells were collected from each sample from the same tissue section and captured on CapSure Macro LCM caps (Arcturus Bioscience, Mountain View, CA). SYN- cells were captured at ≥ 500 μm from the SYN+ cells (Figure S4B). A median of 2000 (range from 700-15,300) SYN+ and 3000 (1,300-16,600) SYN- cancer cells were isolated from six 4 μm sections for each case. Microdissected caps were stored at −80°C until further processed. We have previously demonstrated that this procedure does not affect protein integrity and post-translational modifications providing an excellent enrichment method for downstream analysis of human specimens (Baldelli et al., 2015; Hunt et al., 2020).

Samples were lysed in batches using the QProteome FFPE Tissue kit (Qiagen, Hilden, Germany) supplemented with 6% β-mercaptoethanol as previously reported (Baldelli et al., 2021). In brief, lysis buffer was added to each CapSure Macro LCM Cap. Lysing samples were then placed on ice for 5 min, boiled in a heating block for 20 min, and incubated at 80°C in a water bath for 2 h. Supernatants were collected and stored at −80°C after they were on ice for 1 min and centrifuged at 14,000xg, at 4°C for 15 min.

Reverse phase protein microarray construction and immunostaining

Before array construction, samples were thawed at room temperature and boiled at 100°C for 2 min. Samples were then immobilized onto nitrocellulose-coated glass slides (Grace Bio-labs, Bend, OR) in technical replicates (n = 3) along with a reference standard, and internal controls using a 2470 Quanterix Arrayer (Quanterix, Billerica, MA). Dedicated arrays were stained with Sypro Ruby Protein Blot Stain (Invitrogen, Waltham, MA), following the manufacturer's instruction to assess protein concentration (Baldelli et al., 2017). Briefly, arrays were fixed in a 10% methanol and 7% acetic acid solution for 15 min, washed four times for 5 min in deionized water and incubated with Sypro Ruby Protein Blot Stain for 30 min.

On the day when the immunostaining was performed, remaining arrays were probed with a Reblot Plus Mild Antibody stripping solution for 15 min (Millipore, Burlington, MA), washed in PBS twice, and incubated with in I-block solution (Applied Biosystems, Foster City, CA) for 4 h (Baldelli et al., 2017). Using an automated system (Dako Cytomation, Carpinteria, CA), arrays then were probed with a total of 57 rabbit primary antibodies recognizing unmodified or post-translationally modified epitopes. Primary antibodies were validated before their use as previously reported (Signore et al., 2017). Samples were then probed with a biotinylated anti-rabbit (1:7500, goat, Vector Laboratories, Burlingame, CA) secondary antibody followed by a commercially available tyramide-based detection kit (GenPoint, Agilent, Santa Clara, CA) coupled with the IRDye680 dye (LI-COR Biosciences, Lincoln, NE) (Baldelli et al., 2017). Selected arrays were probed with the secondary antibody only to capture unspecific binding associated with the detection system. Using the proper wavelength channel, antibody, control, and Sypro Ruby Protein Blot-stained slides were imaged using a laser PowerScanner (TECAN, Männedorf, Switzerland) (Baldelli et al., 2017).

QUANTIFICATION AND STATISTICAL ANALYSIS

Image analysis

Image analysis was performed using a commercially available software v5.1.0.0 (Micro-Vigene software, VigeneTech, Inc., Carlisle, MA) as previously reported (Pin et al., 2014). Briefly, the software is designed to automatically perform spot finding, normalization to the amount of protein in each sample, background subtraction, and average between technical replicates.

Statistical analysis

Frequency distribution of nominal variables was assessed using the Fisher's exact test or the chi-square test based on the number of counts in the compared groups. Continuous signal transduction data generated by the RPPA were displayed using unsupervised hierarchical clustering analysis generated in JMP v16 (SAS Institute Inc., Cary, NC) where data were normalized according to the Ward's method. Fold changes were then calculated between matched SYN+ and SYN- clones and RPPA intensity values of the 57 measured proteins were compared between the two clones using a Student's T-test. p values <0.05 were considered significant. RPPA data were displayed using bar graphs, line and boxplots created in GraphPad Prism v. 9.3.0 (GraphPad Software, San Diego, CA). Correlation maps were generated to capture interconnected signaling molecules in the NE+ and NE-clones. Paired Spearman's rank-order correlation coefficients were first calculated across the 57 analytes measured by RPPA in the SYN+ and SYN- clones using JMP v16. Interactions with positive or negative correlation coefficients ≥0.85, suggesting a strong direct or inverse correlation between analytes, were displayed using Gephi v0.9.2, as previously described (Chiechi et al., 2013). In brief, the dimension of each node was designed to be proportional to the number of interconnections of each protein.